JGR Space Physics

RESEARCH ARTICLE
10.1029/2023JA032115

Determination of Outer Radiation Belt MeV Electron Energization Rates and Delayed Response Times to Solar Wind Driving During Geomagnetic Storms

P. Srinivas[1,2] and **E. Spencer**[1]

[1]Electrical and Computer Engineering Department, University of South Alabama, Mobile, AL, USA, [2]Systems Engineering Program, University of South Alabama, Mobile, AL, USA

Key Points:

- The energization rate τ_L and the time delay τ_D between initial dropout and subsequent energization of the electrons consistently increase going from the 1.8–7.7 MeV electron energy bands
- The τ_L and τ_D values are clustered together for each energy level despite the different storm intervals and intensities
- The dropout interval increases with an increase in energy level which was obtained based on sub-storm onsets predicted within the dropout range

Supporting Information:

Supporting Information may be found in the online version of this article.

Correspondence to:

P. Srinivas,
pavithrags@gmail.com

Citation:

Srinivas, P., & Spencer, E. (2024). Determination of outer radiation belt MeV electron energization rates and delayed response times to solar wind driving during geomagnetic storms. *Journal of Geophysical Research: Space Physics*, *129*, e2023JA032115. https://doi.org/10.1029/2023JA032115

Received 26 SEP 2023
Accepted 26 JUN 2024

Author Contributions:

Conceptualization: P. Srinivas, E. Spencer
Data curation: P. Srinivas
Formal analysis: P. Srinivas, E. Spencer
Funding acquisition: E. Spencer
Investigation: P. Srinivas
Methodology: P. Srinivas
Resources: P. Srinivas
Software: P. Srinivas, E. Spencer
Supervision: E. Spencer
Validation: P. Srinivas, E. Spencer
Visualization: P. Srinivas
Writing – original draft: P. Srinivas, E. Spencer
Writing – review & editing: P. Srinivas, E. Spencer

Abstract Radiation Belt Storm Probes (RBSP) data show that seed electrons generated by sub-storm injections play a role in amplifying chorus waves in the magnetosphere. The wave-particle interaction leads to rapid heating and acceleration of electrons from 10's of keV to 10's of MeV energies. In this work, we examined the changes in the radiation belt during geomagnetic storm events by studying the RBSP REPT, solar wind, AL, SML, and Dst data in conjunction with the WINDMI model of the magnetosphere. The field-aligned current output from the model is integrated to generate a proxy E index for various energy bands. These E indices track electron energization from 40 KeV to 20 MeV in the radiation belts. The indices are compared to RBSP data and GOES data. Our proxy indices correspond well to the energization data for electron energy bands between 1.8 and 7.7 MeV. Each E index has a unique empirical loss rate term (τ_L), an empirical time delay term (τ_D), and a gain value, that are fit to the observations. These empirical parameters were adjusted to examine the delay and charging rates associated with different energy bands. We observed that the τ_L and τ_D values are clustered for each energy band. τ_L and τ_D consistently increase going from 1.8 to 7.7 MeV in electron energy flux E_e and the dropout interval increases with increasing energy level. The average trend of $\Delta\tau_D/\Delta E_e$ was 4.1 hr/MeV and the average trend of $\Delta\tau_L/\Delta E_e$ was 2.82 hr/MeV.

1. Introduction

The discovery of the Van Allen belts was in 1957 by Sergei Vernov who utilized Sputnik 2's data and the name of the belts was assigned in honor of James Van Allen for his earlier work with sounding rockets W. Li and Hudson (2019). Since then there have been various studies done on the highly energetic charged particles in inner and outer belts, principally electrons in the higher altitudes and protons in the lower altitudes. Based on the two-zone structure, it was discovered that the outer belt is larger than the inner belt when studying higher-energy electrons and the opposite when studying lower-energy electrons. Wave-particle interactions are the reason for the two-zone structure and they also cause pitch angle scattering loss in the atmosphere. The inner belt is generated from inward diffusion (which contributes to the formation of the outer belt) and the outer belt from acceleration which gives the two-zone structure equilibrium Kim et al. (2011). W. Li and Hudson (2019).

The launch of the Radiation belt storm probes (RBSP) or the Van Allen Probes gives rise to further studies of the radiation belts and Earth's ring current W. Li and Hudson (2019). The radiation levels in the Van Allen belts burst out or simmer depending on the events occurring, including interactions between particles and waves, the Earth's magnetosphere injecting particles into the region, or the solar wind Pokhotelov et al. (2008), Horne et al. (2005), Thorne (2010). These events can lead the radiation levels to escalate drastically to perilous levels in a short period. These increases in radiation levels cause hazardous risks to astronauts and orbiting satellites. Wave particles were discovered before the launch of the Van Allen Probes and the spacecraft provided data that identified several plasma wave properties that disclosed particle fallout drivers from the radiation belts, and relocation of energy between the particles, and helped discover the physics behind the acceleration of killer electrons that disturb satellite operations Spence et al. (2013).

Ultra-relativistic electron production is led by geomagnetic storms through intense substorms which produce waves. These chorus waves rapidly accelerate and heat 10–100s keV seed electrons to higher energies. Wave-particle interactions are prudent in a wide range of energies and essentially in all areas of the magnetosphere D. N. Baker (2021). ULF waves in the other region of the radiation belt can manufacture flux acceleration and modulations Rostoker (1998). The inflation in the trapped relativistic electron flux in approximately half of the

geomagnetic storms in the outer zone is determined by the magnitude of ring current which is carried predominantly by protons at hundreds of keV Reeves et al. (2003). Sudden intensification of inner belt electrons, in the 10–100s of keV energy range, is proposed to be caused by penetration of electric fields and enhanced convection and/or inward radial diffusion. The geomagnetic storms are intermittently related to the creation of several bands of energetic electrons and protons which from 100 keV to multiple MeV range produced from coherent interactions quasi ULF waves with energetic particles. Interactions of electromagnetic waves in the whistler chorus frequency range with seed populations of about 10–200 keV electrons lead to rapid acceleration. Jaynes et al. (2015), Foster et al. (2014), D. N. Baker, Jaynes, Li, et al. (2014).

This paper is based on the observation of coronal mass ejection-driven geomagnetic storm events with varying Dst values. The research started by looking at D. N. Baker et al. (2016) paper where they observed two large storms in 2015 with the Dst value reaching −223 nT. They both produced a total loss of radiation belt high-energy of *EMeV* electron fluxes. The kinetic energy recovering electrons extended up to 10 MeV and strong butterfly distributions with minima flux at $\alpha = 90°$. We used the REPT instrument in the Van Allen Probe satellite which measures protons from $E = 15$ MeV to $E > 100$ MeV and directional characteristics of electrons from approximately 1 to 20 MeV and measures the energy spectrum with good precision and accuracy throughout the higher altitude parts and within inner Van Allen zone during the solar energetic particle events Selesnick et al. (2014, 2016), D. N. Baker et al. (2016). The impenetrable barrier for earthward transport of highly relativistic electrons at $L = 2.8$ is described in D. Baker, Jaynes, Li, et al. (2014). D. N. Baker et al. (2016) referred to three distinct regions regarding highly energetic electrons: the inner radiation belt $L < 2$, the slot region $2 < L < 2.5$, and the outer radiation belt $L > 2.5$.

Most geomagnetic storms can be segregated into three phases namely initial/pre-storm phase, main phase, and recovery phase. The initial phase manifests the classic inner and outer belt structure tens of keV to about 1 MeV electrons. In this phase, at the lower energy, the slot region is broader for electrons and the outer extremity of the inner belt expands to elevated L-shells. In the course of the main phase, in the outer radiation belt region, several hundreds of keV to MeV electrons manifest a dropout behavior. Geomagnetic storms can also be classified as coronal mass ejections driven related to explosive releases of energy from the Sun, co-rotational interaction region, stream interaction region driven based on consistent coronal holes, and high-speed solar wind storms (HSS) driven (Reyes et al., 2021; J. Zhang et al., 2007). Depending on the driving factor, the storms would have varying effects on the radiation belts. For instance, if HSS drives the storm it causes losses, such as the 26–29 September 2017 storm which was a moderate geomagnetic storm with a minimum −74 nT SYM-H caused partial depletion consequentially leading to enhancement of the outer belt at high L shells in the recovery phase of the storm which evolved into three belts stable configuration (Pinto et al., 2018). Recurrent HSS causes high-velocity solar wind which causes lengthy periods of ULF pulsations which lead to high flux production of relativistic electrons by electron acceleration by Pc5 pulsations in the outer radiation belt (Borovsky & Denton, 2006; Mathie & Mann, 2000; O'Brien et al., 2001; G. Rostoker et al., 1998). In the case of CME-driven storms, the impact of sheath and ejecta on radiation belts is quite different (Pokhotelov et al., 2016).

This dropout is possibly accompanied by MeV electron flux recovery which is a consequence of local acceleration substituting on seed populations which is caused by whistler-mode chorus wave interactions throughout substorms and inward radial diffusion Green and Kivelson (2004), Jaynes et al. (2015), Summers et al. (1998), Silva et al. (2022). In the slot region, there is a flood of new electrons in tens to a few hundred keV electrons during the main phase. Finally in the recovery phase, in the majority of the events, the >1 MeV electrons intensify approximately inside the outer radiation belt. During the recovery phase, the slot gets reformed due to the energy-reliant loss depleting the tens to hundreds of keV electrons in the lower L-shells. D. L. Turner et al. (2019), D. Turner et al. (2012), Nikitina and Trichtchenko (2021).

Ganushkina et al. (2005) stated that some of the electron seed population needed particle acceleration to take place inside the inner magnetosphere which was led by substorm activity in the magnetotail from dynamical processes. Magnetic holes are filled with high-energy electrons up to a few hundred keV in the form of huge depressions of magnetic field observed in the vicinity of depolarization fronts by the THEMIS satellites (Balikhin, Sibeck, et al., 2012). The origin and nature of these formations are essential in the comprehension of the string of events that steer the production of high-energy particles in the magnetosphere. The likely causes of magnetic depressions stated by (Balikhin, Sibeck, et al., 2012) are that electrons inside and outside the dips are separated and the high energy electrons supply to maintaining the pressure balance inside these depressions.

Silva et al. (2022) stated that there are multiple reasons for flux dropouts occurrences. The common reason, as mentioned in the previous paragraph is variations of flux in the outer radiation belt that transpires from notable acceleration and loss of electrons, which are generally associated with active geomagnetic conditions. Wave-particle resonant exchanges with multiple elevated frequency plasma waves induce electron precipitation and also cause flux dropouts. Thus, Radial diffusion is a crucial mechanism for steering flux dropouts and radiation belt electron recovery. The multi-MeV electron systems wave-induced precipitation are probably magnified during storms and the consequence of this gives fast localized electron dropouts ascribed to electromagnetic ion cyclotron (EMIC) wave interactions. Silva et al. (2022), Shprits et al. (2017), Summers et al. (1998).

In this work, we establish the timing of the energization of the outer belt during storm periods. We report the relationship between geomagnetic substorms and the fluctuation of trapped relativistic electron fluxes in the outer radiation belts during geomagnetic storms, specifically during the dropout periods. Observations shown in this paper were made during 10 geomagnetic storms from 1.8 to 7.7 MeV electron energy levels.

The structure of this paper is as follows. In the next section, we briefly describe the WINDMI model and the differential equation added to the model that is used to track the energization and time-delayed response of the electrons in the outer radiation belt. We then discuss the data set used, followed by our results. We make some observations in the penultimate section and conclude with a summary of the paper.

2. The WINDMI Model

The plasma physics-based WINDMI model uses the solar wind dynamo voltage, V_{sw}, generated by a particular solar wind-magnetosphere coupling function to drive eight ordinary differential equations describing the transfer of power through the geomagnetic tail, the ionosphere, and the ring current. The model is described in some detail in Doxas et al. (2004), Horton et al. (2005), and more recently, in Spencer et al. (2007). The nonlinear equations of the model trace the flow of electromagnetic and mechanical energy through eight pairs of transfer terms. The remaining terms describe the loss of energy from the magnetosphere-ionosphere system through plasma injection, ionospheric losses, and ring current energy losses. The equations are derived from volume integrals of the plasma momentum and energy equations over the associated regions of the magnetosphere. The coefficients in the differential equations are physical parameters of the magnetosphere-ionosphere system.

The input into the WINDMI model is a voltage that is proportional to a combination of the solar wind parameters measured at L1 by the Advanced Composition Explorer (ACE) satellite. These parameters are the solar wind velocity v_{sw}, the IMF B_x^{IMF}, B_y^{IMF}, B_z^{IMF}, and the solar wind proton density n_{sw}, measured in GSM coordinates are obtained from ACE Magnetic Field 16-Second Level 2 Data and ACE/SWEPAM Solar Wind Experiment 64-Second Level 2 Data instruments obtained from CDAWeb. The input parameters are time delayed to account for the propagation of the solar wind to the nose of the magnetosphere at $10R_E$ as given in Spencer et al. (2007). The input function used for the model is the standard rectified vB_s formula Reiff and Luhmann (1986), given by:

$$V_{sw}^{Bs} = 40(kV) + v_{sw}B_s^{IMF}L_y^{eff}(kV) \quad (1)$$

where v_{sw} is the x-directed component of the solar wind velocity in GSM coordinates, B_s^{IMF} is the southward IMF component and L_y^{eff} is an effective cross-tail width over which the dynamo voltage is produced. For northward or zero B_s^{IMF}, a base viscous voltage of 4 kV is used to drive the system.

The current I_1 used in the model is that portion of the field-aligned region 1 current that maps to the nightside central plasma sheet and is considered to be part of the substorm current wedge that produces the westward auroral electrojet. The Auroral *AL* index now follows as a magnetic field perturbation ΔB_{AL} from the ambient terrestrial field due to the westward electrojet current that flows in the E-layer ($\sim 90 - 120$ km) in the nightside ionosphere. We estimate the relation between I_1 and the *AL* index by assuming that the current I_1 is related linearly to the AL index by a constant of proportionality Spencer et al. (2007).

In this work, we integrate the I_1 field-aligned current to generate a proxy E Index, or Electron Energization Index, incorporating a variable time delay and energy loss rate. This modification is given by the following differential equation, with E representing the E index, as,

$$\frac{dE}{dt} = \alpha U(t - \tau_D) - \frac{E}{\tau_L} \quad (2)$$

This linear differential equation is coupled to the WINDMI model and is used to analyze the energization rates during several geomagnetic storms.

In the above expression, α is a gain applied to the input, U is I1 current (auroral electrojet), τ_D is a delay applied to the input, and τ_L is a loss rate that is assumed to be proportional to the containment time of energetic electrons in the radiation belt. This linear differential equation is coupled to the WINDMI model and is used to study a set of 27 events. In addition, the value of the parameter α is used to adjust the overall gain of the E index in order that it matches the saturation levels of the electron flux energy band under consideration.

We should note that the initial dropout that occurs at the start of the storm is not modeled by the differential equation employed here. This is because the dropout rate is different from the energization rate, which raises the complexity of the model. A modification will be addressed in future work. Here we will focus on establishing the timing of the energization of the outer belt, and how substorm injections impact it.

The E index is compared to RBSP data and GOES data. We initially analyzed a data set of 27 magnetic storms from the year 2012–2018. These events occurred over diverse durations and were of different intensities. The model was tuned along with the SML index and the AL index. From the 27 events, 10 storms were selected for further analysis. These were 21–29 June 2015, 6–9 September 2017, 5–12 October 2015, 7–12 November 2017, 6–13 February 2014, 17–27 March 2015, 23–31 October 2016, 31st October–2nd November 2012, 16–18 March 2013, and 25–28 August 2018. The storms that were not chosen were 18–22 February 2014, 27–28 February 2014, 29 April–1 May 2014, 26–30 August 2014, 12–14 September 2014, 9–12 April 2015, 7–10 June 2015, 4–8 July 2015, 22–25 July 2015, 8–10 September 2015, 19–21 September 2015, 6–8 November 2015, 7–11 May 2016, 31 December 2015–2 January 2016, 27–30 May 2017, 16–20 July 2017, 26–29 September 2017, 19–22 April 2018. All 27 storms were categorized by the maximum Dst value and for this study it was decided to chose a set of storms that have wide range of maximum Dst values (ranging from −35 to −222) in order to test extreme storm cases. The storms that were not chosen had intemediate values of maximum Dst ranging from −63 to −125 (Tsagouri & Belehaki, 2023).

3. Data Set

The Van Allen Probes or the RBSP which is composed of two identically equipped satellites that were launched to study the Van Allen belts surrounding the Earth. They orbit Earth in an elliptical orbit with an apogee of 30,414 km and a perigee of 618 km. They have the ability to measure charged particle populations, waves, and fields. One of the sensors onboard is ECT (Energetic Particle Composition and Thermal Plasma Suite). ECT gives the temporal, spatial, and pitch angle distributions of ions and electrons over an extensive range of energies. The ECT suite encompasses three sensor sets, namely Magnetic Electron Ion Spectrometer, Helium Oxygen Proton Electron, and REPT (Relativistic Electron Proton Telescope). The data used for this study is from the RBSP ECT REPT Level 2 science data. Specifically, the Spin-Averaged Differential Electron Flux 2–20 MeV, in 12 energy bands is used. REPT measures the electrons at 25% resolution [15]. Out of the available energy levels, data from 1.8 to 7.7 MeV was used after the elimination of other cumbersome data.

The ACE satellite is positioned at Sun-Earth L1 Lagrange point at 870,000 mi from Earth to study and measure, magnetic fields, particles, and near-real-time solar wind. Magnetic field vector in GSM coordinates (16 s) and time was taken from H0 to ACE Magnetic Field 16-Second Level 2 Data. Solar Wind Proton Number Density, scalar, Solar Wind Velocity in GSM coord., 3 comp, and time was taken from ACE/SWEPAM Solar Wind Experiment 64-Second Level 2 Data. These parameters are provided as inputs to the WINDMI model. The magnetic field vectors taken at every 16 s and solar wind velocity values taken at every 64 s are essential for all studies performed in this work.

AL index portrays the powerful current intensities of the westward auroral electrojet which is measured in the auroral zone by a particular network of magnetometers [19]. The SML index is derived based on the AL index given in [20]. AL index data is obtained from the World Data Center for Geomagnetism, Kyoto in the IAGA-2002 format in provisional data type at 1-min data intervals. The SML index data is obtained from the SuperMAG site

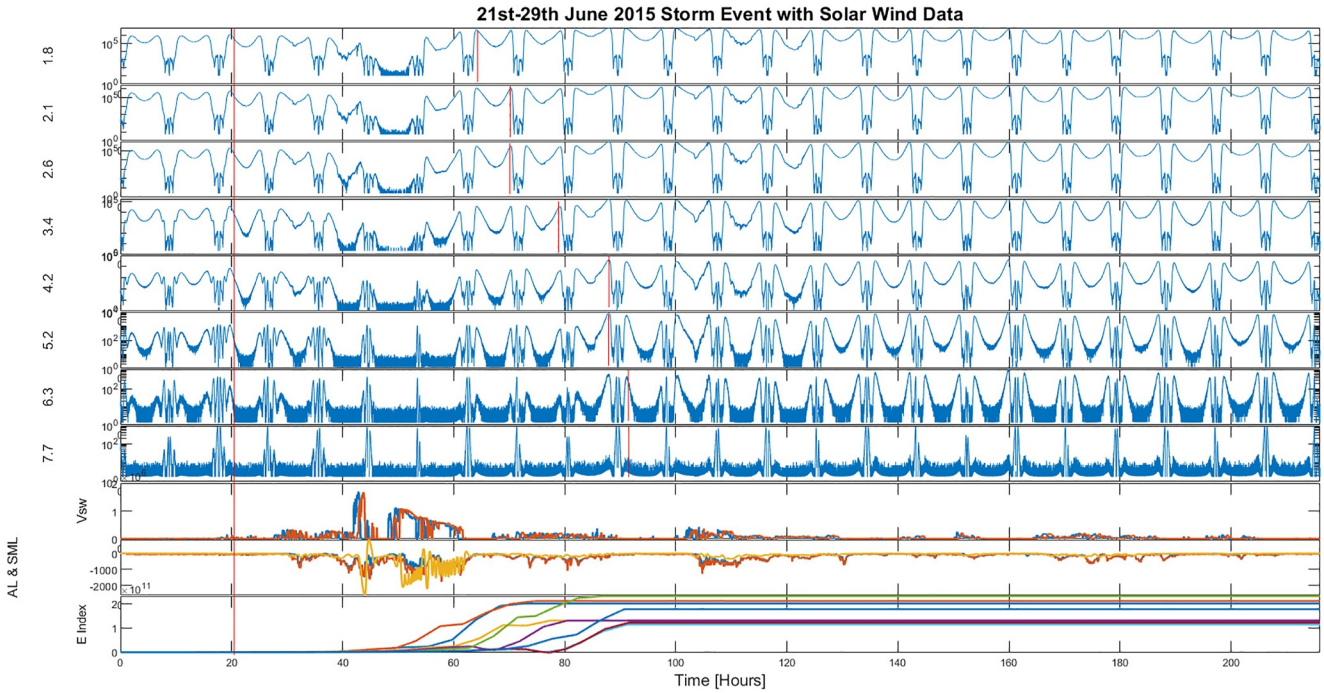

Figure 1. 21st June 2015 to 29 June 2015 from 1.8 to 7.7 MeV from RBSP satellite. This storm lasted for 9 days. The E index curve is pushed up to about the same time as the RBSP REPT data from the beginning of when the solar wind starts and stays up till the end of the storm time. The first red line running down the first eight panels represents the start of the dropout and the second red line is individually marked to represent the end of the dropout for each energy level. There is a clear increase in the dropout gap with the increase in energy level as seen in the first eight panels. The common dropout region for all the energy levels matches the peak in solar wind velocity. The E index curves are adjusted to match the RBSP REPT energy level after dropout curves as shown in the last panel.

at 1-min data intervals. SuperMAG is a collaboration of worldwide organizations providing data from close to 600 ground based magnetometers with easy access to perturbations data magnetic field in same coordinate system with similar time resolution (Gjerloev, 2009, 2012).

Between the years 2012 and 2018 (due to the availability of data), multiple storms were analyzed and 10 storms were chosen based on Kp index value, intensity, and duration. The 10 storms are categorized into three energy levels with respect to the RBSP data namely 1.8 MeV, 2.1 MeV, 2.6 MeV, 3.4 MeV, 4.2 MeV, 5.2 MeV, 6.3 MeV, and 7.7 MeV. In each of these 10 cases, the first eight panels in Figure 1 on page 16 and respective figures of other storms show the RBSP energy levels. The ninth panel shows the solar wind input voltage shifted from L1 to the magnetosphere in rate. The tenth panel shows the AL index, SML index, and WINDMI output. The eleventh panel has the WINDMI output adjusted with respect to the RBSP data in the first eight panels in Figure 1 on page 16.

The 10 storms were analyzed with respect to the SML index during the time. For better analysis, two to 5 days before and after the storm time was taken to observe how long the storm lasted. Ten of these storms were selected based on fixed criteria. The criteria included that the events selected correlated well with the SML index and had RBSP data available for comparison. The 10 storms selected were 21–29 June 2015, 6–9 September 2017, 5–12 October 2015, 23–31 October 2016, 7–12 November 2017, 17–27 March 2015, 6–13 February 2014, 31st October–2nd November 2012, 16–18 March 2013, and 25–28 August 2018.

4. Results

For this paper, 10 storms data were chosen from the Space Weather live website which gives the list of the top 50 geomagnetic of each year with respect to the Ap index and Kp index, and Kakioka Magnetic Observatory Geomagnetic Storm Catalog. To obtain the E index, the ACE data was used as input into the WINDMI model, and the model's code was modified to provide the E index as the output along with the solar wind velocity AL index and SML index. The E index part of the code has the gain factor α, τ_L, and τ_D which is altered according to the required E index output. The time in the x-axis is in hours. The E-index is modified to match the signature of the RBSP REPT output curve. The RBSP REPT output curve is obtained from the NASA CDA website. This file is

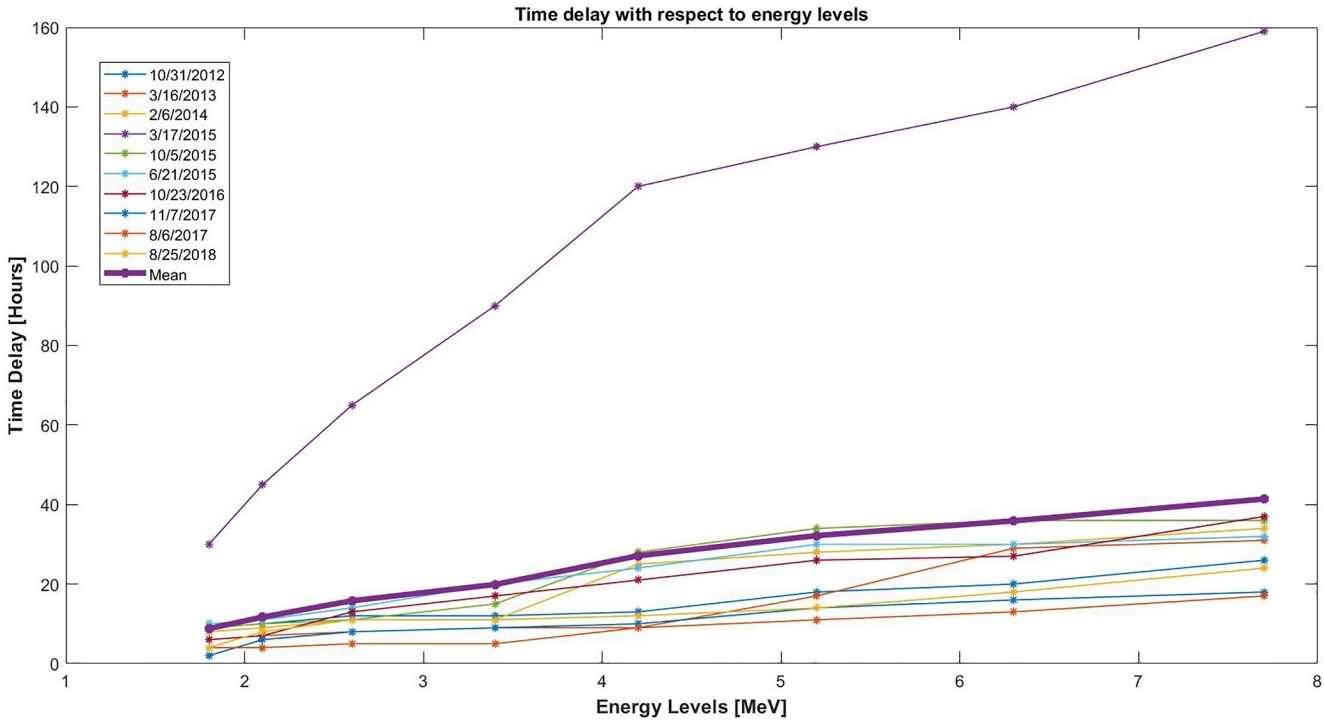

Figure 2. This graph shows the τ_D or time delay [Hours] curves for each storm event with respect to energy levels [MeV]. The stray curve is the 17th–27th March 2015 storm event which had abnormally high values of τ_D compared to the other events and hence was classified as the outlier. The mean of all the curves is denoted by the dark purple curve. The $\Delta\ \tau_D/\Delta E_e$ value derived from the mean curve is 6.31 when the outlier storm is included.

then processed to be able to read the data and display it. The unusable parts of the data are averaged out to give smooth curves without breaks. The final output data plots are provided in the supplementary section. This process applies to all the data sets. We examined energy levels from 40 to 400 keV of GOES data and 1.8–20 MeV of RBSP data. The GOES data was dropped out of the observations presented in this paper due to a lack of unusable data evenly available for the entire data set. It was difficult to notice patterns in the data as compared to the RBSP 1.8–7.7 MeV data. The GOES data from 40 to 400 keV will be further analyzed using existing GOES satellite data comparison methods such as (Pokhotelov et al., 2016) for further studies.

The most noticeable change in data during storm time which helped to categorize the storm into initial, main, and recovery phases are 1.8–7.7 MeV energy levels. Separate E indices were created for each energy level and have their own τ_L, τ_D, and gain parameters. Each of these parameters was varied corresponding to the activity happening at particular energy levels. The tables that contain τ_L, τ_D, and electron flux saturation values that were varied are given in the supplementary section. Also, the supplementary section contains all 10 of the geomagnetic storm result graphs with the E index adjusted except for the 21st–29th June 2015 storm. In the Figure 2 on page 17, curves for all 10 storm events are presented with respect to 1.8–7.7 MeV energy levels. The stray curve is the 17th–27th March 2015 storm event which had abnormally high values of τ_D compared to the other events and hence was classified as the outlier. Thus, after removing the outlier, Figure 4 on page 19 shows the curves together to form a frustum envelope shape. The steady increase in τ_D with the increase in energy level is observed. Similarly, Figure 3 on page 18 all 10 storm events are presented with respect to 1.8–7.7 MeV energy levels. The two stray curves are the 5th–11th October 2015 storm event and the 31 October–2 November 2012 which had abnormally low values of τ_L compared to the other events and hence were classified as the outliers. Thus, after removing the outliers, Figure 5 on page 20 shows the curves are within a specific range of each other and the curves together form a frustum envelope shape. There is a steady increase in τ_L with the increase in energy level. Since the points/values are closer together than the τ_D, it makes the τ_L value easier to predict. The supplementary file has the graphs for the same values of τ_D and τ_L with respect to time. This is shown by observing the data through the years and note changes through the solar cycle.

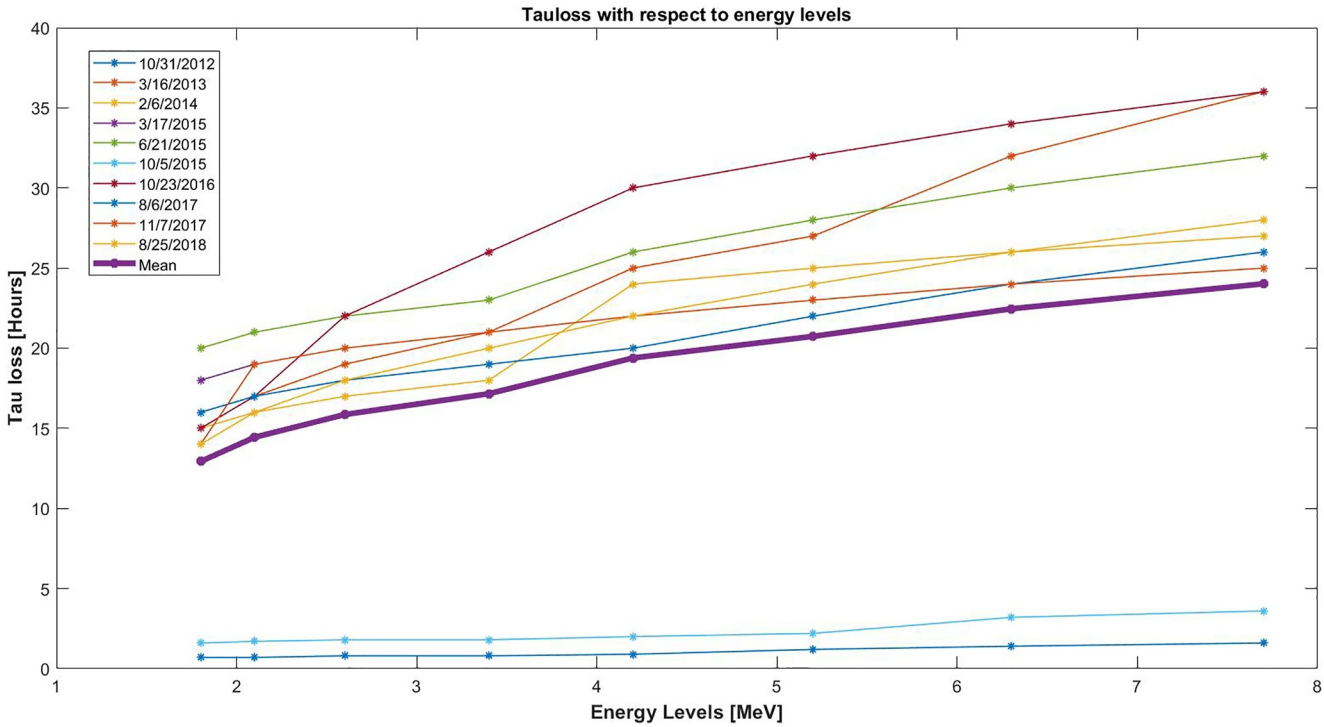

Figure 3. This graph shows the τ_L [Hours] curves for each storm event with respect to energy levels [MeV]. The two stray curves are the 5th–11th October 2015 storm event and the 31 October–2 November 2012 which had abnormally low values of τ_L compared to the other events and hence were classified as the outlier. The mean of all the curves is denoted by the dark purple curve. The $\Delta\ \tau_L/\Delta E_e$ value derived from the mean curve is 2.28 when the outlier storms are included.

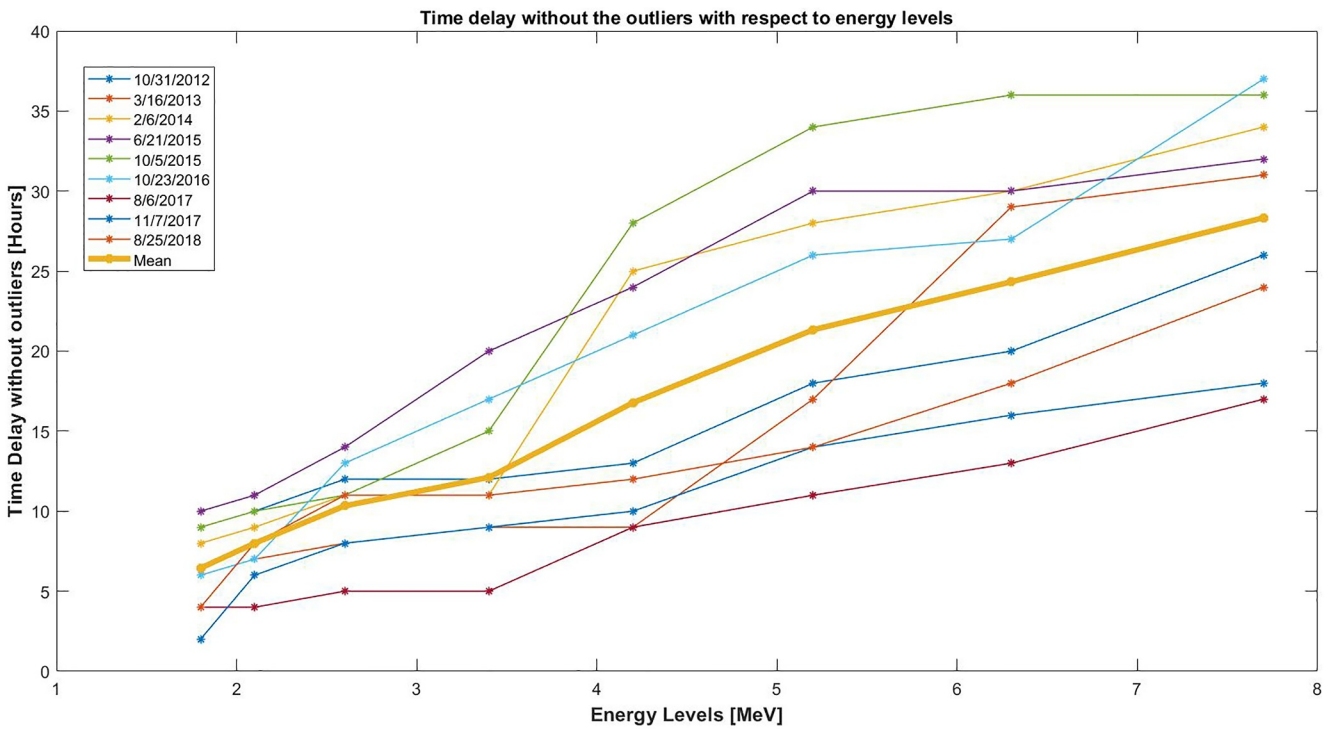

Figure 4. This graph shows the τ_D or time delay [Hours] curves for each storm event with respect to energy levels [MeV] without the outliers. As seen in the plot, the points in each energy level are within a specific range of each other thus the lines together form a frustum envelope shape. There is a steady increase in τ_D with the increase in energy level. The mean of all the curves is denoted by the yellow curve. The $\Delta\tau_D/\Delta E_e$ value derived from the mean curve is 4.1 when the outlier storm is excluded.

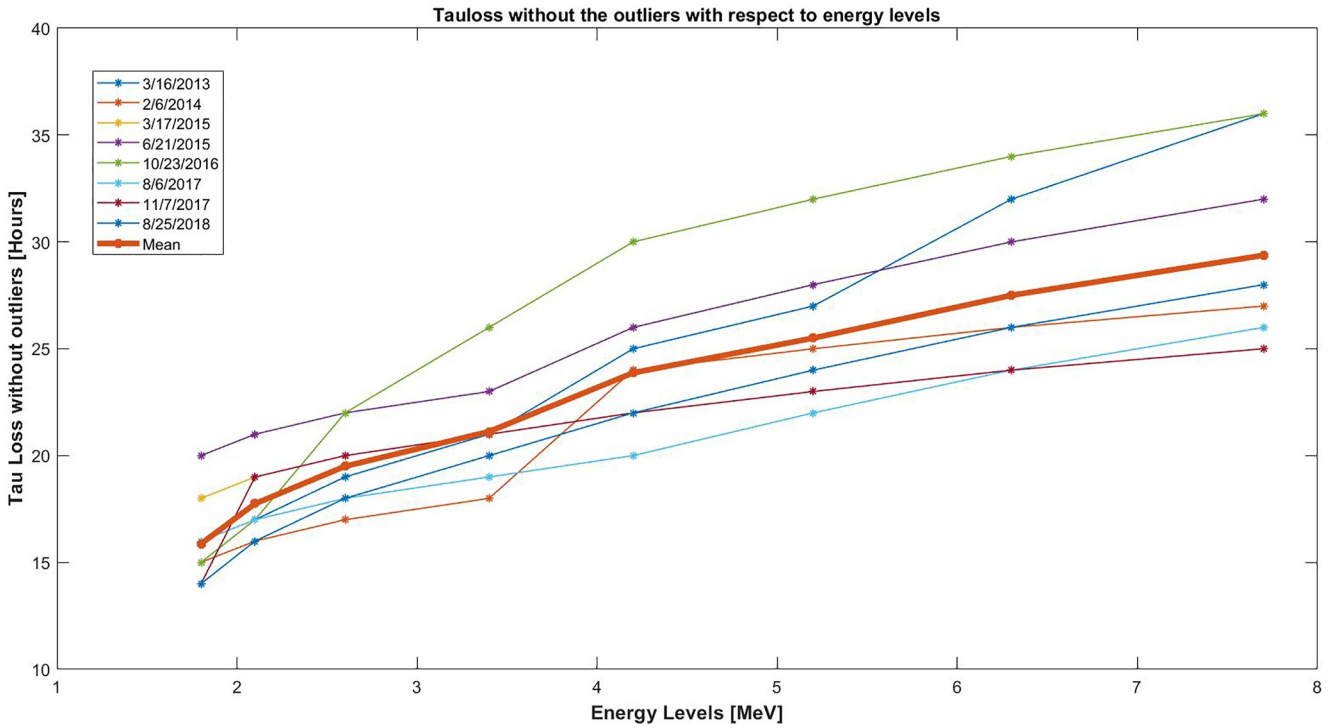

Figure 5. This graph shows the τ_L [Hours] curves for each storm event with respect to energy levels [MeV] without the outliers. As seen in the plot, the points in each energy level are within a specific range of each other thus the lines together form a frustum envelope shape. There is a steady increase in τ_L with the increase in energy level. Since the points/values are closer together than the τ_D, it makes the τ_L value easier to predict. The mean of all the curves is denoted by the red curve. The $\Delta\tau_D/\Delta E_e$ value derived from the mean curve is 2.82 when the outlier storms are excluded.

The τ_D is marked as the start of the injection based on the AL and SML index, signaling the starting point of pumping seed electrons into the near-earth tail region of the magnetosphere. The τ_D was varied based on when the observed injection would pick up after the dropout in the respective RBSP energy level data. The τ_L is the charging time that was adjusted concerning the variation in the curve pattern as observed in the respective RBSP energy levels. The E Index curve is adjusted by varying the τ_D and τ_L. The gain is kept constant for this study. Thus the E Index is set to follow the RBSP REPT data curve closely. The best-adjusted values of τ_D and τ_L that work with our model are given in Table 1. Two outliers were identified for τ_L and one outlier was identified for τ_D. The 17–27 March 2015 was the outlier for τ_D study and the possible reason for that is that particular storm had the highest minimum Dst, maximum flux density, and high Kp value compared to the rest of that data set. Further studies on these outliers will be conducted in the future. These graphs were plotted against both the energy levels and time to detect patterns. We see a clear rise in the values in all storm cases with increasing electron energy levels.

As shown in 4 on page 19, a mean of all τ_D curves from the storm set is taken, and a curve is formed by connecting all the mean points. Similarly, a mean curve is created for τ_L as in 5 on page 20. The mean curve represents the general trend in both cases. In the case of τ_D, the average value of the rate of change of the time delay per unit electron energy flux is represented by $\Delta\tau_D/\Delta E_e$. This average rate is approximately 4.1 MeV per hour when the outlier storm is not included. For τ_L, the mean value of the rate of change of the containment time per unit electron energy flux is $\Delta\tau_L/\Delta E_e$. The average rate is approximately 2.82 MeV per hour. The mean values were calculated using the equation stated below where the X term is either the τ_L or τ_D values in the increasing order of energy level, the Y term is the energy level values in the increasing order, and n represents the position of energy levels in increasing order. We used mean values here and therefore, implicitly assumed that the energization rates and time delays were normally distributed (Table 2).

$$M = \frac{1}{n}\left[\frac{(Y_2 - Y_1)}{(X_2 - X_1)} + \frac{(Y_3 - Y_2)}{(X_3 - X_2)} + \cdots + \frac{(Y_n - Y_{n-1})}{(X_n - X_{n-1})}\right] \quad (3)$$

Table 1
Table of Events

Storm duration	Energy level (MeV)	τ_L (hrs)	τ_D (hrs)	Flux saturation level	Kp	Max magnetic field (nT)	Duration of storm (hrs)	Dropout duration (hrs)	Total substorms during storm-time	Substorm count during dropout	Dropout
21–29 June 2015	1.8	20	10	21	7	−1,800	9 Days	29	51	10	19.60%
	2.1	21	11	24		−1,800		31		10	19.60%
	2.6	22	14	20		−1,800		38		13	25.49%
	3.4	23	20	20		−1,800		40		14	27.45%
	4.2	26	24	36		−1,800		47		21	41.17%
	5.2	28	30	28		−1,800		47		21	41.17%
	6.3	30	30	34		−1,800		47		21	41.17%
	7.7	32	32	40		−1,800		47		21	41.17%
6–9 September 2017	1.8	16	4	9	5	−1,200	4 Days	36	25	8	32%
	2.1	17	4	10		−1,200		36		8	32%
	2.6	18	5	10.5		−1,200		36		8	32%
	3.4	19	5	16		−1,200		55		12	48%
	4.2	20	9	16		−1,200		61		15	60%
	5.2	22	11	19		−1,200		61		15	60%
	6.3	24	13	19		−1,200		63		15	60%
	7.7	26	17	25		−1,200		72		15	60%
5–12 October 2015	1.8	1.6	9	1.65	6	−2,100	8 Days	35	106	22	20.75%
	2.1	1.7	10	1.3		−2,100		35		22	20.75%
	2.6	1.8	11	2.1		−2,100		38		23	21.69%
	3.4	1.8	15	2.2		−2,100		44		26	24.52%
	4.2	2	28	2.4		−2,100		68		40	37.73%
	5.2	2.2	34	3.2		−2,100		74		42	39.62%
	6.3	3.2	36	6		−2,100		77		45	42.45%
	7.7	3.6	36	7.4		−2,100		77		45	42.45%
7–12 November 2017	1.8	14	2	3.8	5	−1,570	6 Days	36	81	26	32.09%
	2.1	19	6	4.7		−1,570		41		27	33.33%
	2.6	20	8	5.5		−1,570		41		27	33.33%
	3.4	21	9	6.5		−1,570		45		29	35.80%
	4.2	22	10	7.5		−1,570		45		29	35.80%
	5.2	23	14	10		−1,570		45		29	35.80%
	6.3	24	16	12		−1,570		50		34	41.97%
	7.7	25	18	14		−1,570		52		36	44.44%
6–13 February 2014	1.8	15	8	3.3	5	−888	8 Days	74	56	25	44.64%
	2.1	16	9	3.4		−888		84		28	50%
	2.6	17	11	4.7		−888		102		35	62.50%
	3.4	18	11	5		−888		107		39	69.64%
	4.2	24	25	8		−888		125		41	73.21%
	5.2	25	28	9		−888		130		44	78.57%
	6.3	26	30	10		−888		130		44	78.57%
	7.7	27	34	12		−888		130		44	78.57%

Table 1
Continued

Storm duration	Energy level (MeV)	τ_L (hrs)	τ_D (hrs)	Flux saturation level	Kp	Max magnetic field (nT)	Duration of storm (hrs)	Dropout duration (hrs)	Total substorms during storm-time	Substorm count during dropout	Dropout
17–27 March 2015	1.8	18	30	10.5	7	−2,125	10 Days	27	100	27	27%
	2.1	19	45	11		−2,125		36		36	36%
	2.6	20	65	11.5		−2,125		47		47	47%
	3.4	21	90	13		−2,125		49		49	49%
	4.2	22	120	15		−2,125		68		68	68%
	5.2	23	130	17		−2,125		70		70	70%
	6.3	24	140	20		−2,125		80		80	80%
	7.7	25	159	25		−2,125		80		80	80%
23–31 October 2016	1.8	15	6	5.2	5	−1,695	9 Days	56	119	56	15.96%
	2.1	17	7	5.75		−1,695		60		60	19.32%
	2.6	22	13	7.5		−1,695		67		67	26.05%
	3.4	26	17	8		−1,695		71		71	27.73%
	4.2	30	21	9		−1,695		74		74	31.09%
	5.2	32	26	12		−1,695		74		74	37.81%
	6.3	34	27	13		−1,695		96		96	37.81%
	7.7	36	37	18		−1,695		116		116	57.14%
31st October–2nd November 2012	1.8	0.7	9	0.4	5	−1,700	3 Days	35	20	14	70%
	2.1	0.7	10	0.4		−1,700		35		14	70%
	2.6	0.8	12	0.5		−1,700		36		14	70%
	3.4	0.8	12	0.6		−1,700		36		14	70%
	4.2	0.9	13	0.7		−1,700		36		14	70%
	5.2	1.2	18	1.1		−1,700		43		14	70%
	6.3	1.4	20	1.4		−1,700		45		14	70%
	7.7	1.6	26	2		−1,700		52		14	70%
16–18 March 2013	1.8	15	6	6	6	−2,475	3 Days	13	28	13	46.42%
	2.1	17	7	6.75		−2,475		14		14	50%
	2.6	19	8	8.5		−2,475		14		14	50%
	3.4	21	9	8.5		−2,475		14		14	50%
	4.2	25	9	14		−2,475		14		14	50%
	5.2	27	17	16		−2,475		14		14	50%
	6.3	32	29	20		−2,475		14		14	50%
	7.7	36	31	24		−2,475		14		14	50%
25–28 August 2018	1.8	14	4	6	6	−2,165	4 Days	20	34	15	44.11%
	2.1	16	8	6.75		−2,165		26		18	52.94%
	2.6	18	11	8.5		−2,165		29		19	55.88%
	3.4	20	11	8.5		−2,165		35		19	55.88%
	4.2	22	12	14		−2,165		35		19	55.88%
	5.2	24	14	16		−2,165		38		19	55.88%
	6.3	26	18	20		−2,165		44		21	61.76%
	7.7	28	24	24		−2,165		56		26	76.47%

Table 2
Result Table

Parameters	M	STD
$\Delta\tau_L/\Delta E_e$	2.28	9.2
$\Delta\tau_D/\Delta E_e$	6.31	26.26
$\Delta\tau_L/\Delta E_e$ without outliers	2.82	2.9
$\Delta\tau_D/\Delta E_e$ without outliers	4.1	5.44

5. Observations

For the purposes of this analysis, we refer to three distinct regions regarding highly energetic electrons the inner radiation belt ($L < 2$), the slot region ($2 < L < 2.5$), and the outer radiation belt ($L > 2.5$) (D. N. Baker et al., 2016). Analysis of REPT and other Van Allen Probes data showed that there have been no measurable fluxes of $E \geq 1$ MeV electrons in the inner radiation belt region. The energy range we modified the τ_L and τ_D values for the event list was from 1.8 to 7.7 MeV.

In both τ_L and τ_D without outlier graphs, the points in each energy level are within a specific range of each other thus the lines together form a frustum envelope shape. The standard deviation for each energy level cluster of points was calculated. In comparison to the τ_D, the τ_L is more tightly clustered. τ_L seemed more predictable than the τ_D as it had a smaller standard deviation as compared to the τ_D. The same concept applies to the mean values. The values of $\Delta\tau_L/\Delta E_e$ and $\Delta\tau_D/\Delta E_e$ without outliers are lower with the elimination of outliers.

To compare the results with (Balikhin, Gedalin, et al., 2012) we use the storm which is shown in Figure 1. According to the (Balikhin, Gedalin, et al., 2012), the example stated was that if standard diffusion is similar to the square root of time, one day to accelerate a seed population to energies of about 172.5 keV it should take about 25 days to reach 900 keV. The timescale of the widening of the distribution function, according to the standard diffusion equation, should be similar to the square root of time. The time obtained in (Balikhin, Gedalin, et al., 2012) is 10 times faster than the diffusion speed. In the case of energy level 1.8 MeV with respect to 172.5 keV the diffusion would be about 100 days and with 10 times faster observations would be 10 days. The times obtained in this work are much faster than that according to the dropout duration times in Table 1 which in the case of 21st–29th June 2015 would be an average of 1.69 days for 1.8–7.7 MeV. The average across all the storms for all observed energy levels is 2.18 days. Balikhin, Gedalin et al. (2012) obtained a time scale of energization about 10 times faster than the standard diffusion timescale. In this work looking at energy ranges from 1.8 to 7.7 MeV across all data sets, we see that it should be on average 38.35 times faster for the 21st–29th June 2015 storm and similar results across the storms in the supplementary files. In (X. Li et al., 2005), the authors look at events that take place over longer periods of time (180 days at a time). Those results are not comparable to our work which involves observing storm intervals that occur over roughly 10 days.

We observe that the flux dropout interval varies with different energy levels. It increases with the increase in energy level consistently in all storm cases. The vertical red lines indicate the dropout range in the statistics. The number of substorms during the storm time, during the main phase, and the dropout range were observed. The dropout substorm percentage was calculated based on the number of substorms that occurred during the dropout versus the total number of substorms that occurred during storm time. The total number of substorms was obtained from Forsyth's list and then the list was further condensed by picking the substorms that occurred when the Dst index was zero or in the negative value range. The dropout percentages are given in Table 1.

6. Summary

For this study, we focused on establishing the timing of the energization of the outer belt during storm periods, and how substorm injections impact it. We examined 10 geomagnetic storms from 1.8 to 7.7 MeV energy levels for change in electron flux activity during storm periods. For this investigation, we added a linear differential equation to the WINDMI model, including gain, time delay, and loss rate terms. The data from RBSP REPT and ACE were run through the modified version of the WINDMI model and the τ_D and τ_L values were varied for each storm and energy level. The notable results were that the τ_L and τ_D values consistently increased with the energy level. The values were also found to be clustered for the respective energy levels which was proved using the standard deviation values. Since the τ_L had smaller values of standard deviation than τ_D, it was established as more predictable/accurate than τ_D. We also performed an inspection of flux dropouts during the storm period, specifically on the dropout intervals. We detected that the dropout intervals increased with an increase in energy level number and this observation was consistent with the entire data set studied.

In our analysis, we calculated the values of $\Delta\tau_D/\Delta E_e$ and $\Delta\tau_L/\Delta E_e$, the average change in τ_L and τ_D with respect to a change in electron energy level. $\Delta\tau_L/\Delta E_e$ is a measure of how rapidly each electron energy band changes up to its pre-storm levels. $\Delta\tau_D$ is a measure of how long it takes for each energy band to start charging up to its pre-

storm levels. $\Delta\tau_D/\Delta E_e$ linear trend from 4 on page 19 is 4.1. $\Delta\tau_L/\Delta E_e$ linear trend from 5 on page 20 is 2.82. These values are useful measures that can guide modeling and simulation efforts of future studies of the radiation belts during geomagnetic activity. We additionally, calculated the dropout percentages to detect the connection between dropout and storm-time substorm injections. We could not draw any specific conclusive evidence connecting dropouts with storm-time substorm injections for the electron energy fluxes greater than 1 MeV.

Data Availability Statement

All the data used in this research is publicly available at the NASA Space Physics Data Facility at (NASA, 2023). SML data is available from the SuperMAG website (SuperMAG, 2023). The AL data is available from the (WDC, 2023) Kyoto WDC website. The WINDMI model is available for runs on request at the NASA Community Coordinated Modeling Center website. The specific version of the model used for this research is available on GitHub at https://github.com/PavithraGS/WindmiModel. The link to the GitHub data/software to Zenodo is 10.5281/zenodo.11133963 (Srinivas, 2024).

Acknowledgments

We acknowledge Van Allen Probes REPT, ACE Magnetic Field 16-Second Level 2 Data, ACE/SWEPAM Solar Wind Experiment 64-Second Level 2 Data, GOES-15 EPS (Energetic Particle Sensor) MagED (Magnetospheric Electron Detector) 1-min electron fluxes 40–475 keV–NOAA NGDC and SWPC data obtained from https://cdaweb.gsfc.nasa.gov/cgi-bin/eval2.cgi (NASA Goddard Space Flight Center Space Physics Data Facility (SPDF) CDAWeb data sets). We greatly appreciate the SuperMAG collaborators (https://supermag.jhuapl.edu//info/?page=acknowledgement) for the SML index data. We acknowledge the substorm timing list identified by the SOPHIE technique (Forsyth et al., 2015), the SMU and SML indices (Newell & Gjerloev, 2011); and the SuperMAG collaboration (Gjerloev, 2012). We also would like to thank the World Data Center for Geomagnetism, Kyoto, for providing the AL index (http://wdc.kugi.kyoto-u.ac.jp/aeasy/index.html). This study is supported by cooperative agreement NSF RII Track-1: Future Technologies and Enabling Plasma Processes OIA-2148653 and cooperative agreement NSF RII Track-1: CPU2AL: Connecting the Plasma Universe to Plasma Technology in Alabama OIA-1655280.

References

Baker, D., Jaynes, A., Hoxie, V., Thorne, R., Foster, J., Li, X., et al. (2014a). An impenetrable barrier to ultra-relativistic electrons in the Van Allen radiation belt. *Nature*, *515*(7528), 531–534. https://doi.org/10.1038/nature13956

Baker, D. N. (2021). Wave–particle interaction effects in the Van Allen belts. *Earth Planets and Space*, *73*(1), 189. https://doi.org/10.1186/s40623-021-01508-y

Baker, D. N., Jaynes, A. N., Kanekal, S. G., Foster, J. C., Erickson, P. J., Fennell, J. F., et al. (2016). Highly relativistic radiation belt electron acceleration, transport, and loss: Large solar storm events of march and June 2015. *Journal of Geophysical Research: Space Physics*, *121*(7), 6647–6660. https://doi.org/10.1002/2016JA022502

Baker, D. N., Jaynes, A. N., Li, X., Henderson, M. G., Kanekal, S. G., Reeves, G. D., et al. (2014). Gradual diffusion and punctuated phase space density enhancements of highly relativistic electrons: Van Allen probes observations. *Geophysical Research Letters*, *41*(5), 1351–1358. https://doi.org/10.1002/2013GL058942

Balikhin, M. A., Gedalin, M., Reeves, G. D., Boynton, R. J., & Billings, S. A. (2012). Time scaling of the electron flux increase at geo: The local energy diffusion model vs observations. *Journal of Geophysical Research: Space Physics*, *117*(A10). https://doi.org/10.1029/2012JA018114

Balikhin, M. A., Sibeck, D. G., Runov, A., & Walker, S. N. (2012). Magnetic holes in the vicinity of dipolarization fronts: Mirror or tearing structures? *Journal of Geophysical Research: Space Physics*, *117*(A8). https://doi.org/10.1029/2012JA017552

Borovsky, J. E., & Denton, M. H. (2006). Differences between CME-driven storms and CIR-driven storms. *Journal of Geophysical Research: Space Physics*, *111*(A7). https://doi.org/10.1029/2005JA011447

Doxas, I., Horton, W., Lin, W., Seibert, S., & Mithaiwala, M. (2004). A dynamical model for the coupled inner magnetosphere and tail. *IEEE Transactions on Plasma Science*, *32*(4), 1443–1448. https://doi.org/10.1109/TPS.2004.833388

Forsyth, C., Rae, I. J., Coxon, J. C., Freeman, M. P., Jackman, C. M., Gjerloev, J., & Fazakerley, A. N. (2015). A new technique for determining Substorm Onsets and Phases from Indices of the Electrojet (SOPHIE). *Journal of Geophysical Research: Space Physics*, *120*(12), 10592–10606. https://doi.org/10.1002/2015JA021343

Foster, J. C., Erickson, P. J., Baker, D. N., Claudepierre, S. G., Kletzing, C. A., Kurth, W., et al. (2014). Prompt energization of relativistic and highly relativistic electrons during a substorm interval: Van Allen probes observations. *Geophysical Research Letters*, *41*(1), 20–25. https://doi.org/10.1002/2013GL058438

Ganushkina, N. Y., Pulkkinen, T. I., & Fritz, T. (2005). Role of substorm-associated impulsive electric fields in the ring current development during storms. *Annales Geophysicae*, *23*(2), 579–591. https://doi.org/10.5194/angeo-23-579-2005

Gjerloev, J. W. (2009). A global ground-based magnetometer initiative. *Eos, Transactions American Geophysical Union*, *90*(27), 230–231. https://doi.org/10.1029/2009EO270002

Gjerloev, J. W. (2012). The SuperMAG data processing technique. *Journal of Geophysical Research: Space Physics*, *117*(A9). https://doi.org/10.1029/2012JA017683

Green, J. C., & Kivelson, M. (2004). Relativistic electrons in the outer radiation belt: Differentiating between acceleration mechanisms. *Journal of Geophysical Research*, *109*(A3). https://doi.org/10.1029/2003ja010153

Horne, R. B., Thorne, R. M., Shprits, Y. Y., Meredith, N. P., Glauert, S. A., Smith, A. J., et al. (2005). Wave acceleration of electrons in the Van Allen radiation belts. *Nature*, *437*(7056), 227–230. https://doi.org/10.1038/nature03939

Horton, W., Mithaiwala, M., Spencer, E., & Doxas, I. (2005). WINDMI: A family of physics network models for storms and substorms. In A. Lui, Y. Kamide, & G. Consolini (Eds.), *Multiscale coupling of sun-earth processes* (pp. 431–445). Elsevier Science B.V. https://doi.org/10.1016/B978-044451881-1/50032-0

Jaynes, A. N., Baker, D. N., Singer, H. J., Rodriguez, J. V., Loto'aniu, T. M., Ali, A. F., et al. (2015). Source and seed populations for relativistic electrons: Their roles in radiation belt changes. *Journal of Geophysical Research: Space Physics*, *120*(9), 7240–7254. https://doi.org/10.1002/2015JA021234

Kim, K.-C., Lee, D.-Y., Shprits, Y., Kim, H.-J., & Lee, E. (2011). Electron flux changes in the outer radiation belt by radial diffusion during the storm recovery phase in comparison with the fully adiabatic evolution. *Journal of Geophysical Research: Space Physics*, *116*(A9). https://doi.org/10.1029/2011JA016642

Li, W., & Hudson, M. (2019). Earth's Van Allen radiation belts: From discovery to the Van Allen probes era. *Journal of Geophysical Research: Space Physics*, *124*(11), 8319–8351. https://doi.org/10.1029/2018JA025940

Li, X., Baker, D. N., Temerin, M., Reeves, G., Friedel, R., & Shen, C. (2005). Energetic electrons, 50 keV to 6 MeV, at geosynchronous orbit: Their responses to solar wind variations. *Space Weather*, *3*(4). https://doi.org/10.1029/2004SW000105

Mathie, R. A., & Mann, I. R. (2000). A correlation between extended intervals of ULF wave power and storm-time geosynchronous relativistic electron flux enhancements. *Geophysical Research Letters*, *27*(20), 3261–3264. https://doi.org/10.1029/2000GL003822

NASA SC. (2023). NASA goddard space Flight center space physics data facility (SPDF) CDAWeb datasets [Dataset]. https://cdaweb.gsfc.nasa.gov/cgi-bin/eval2.cgi

Newell, P. T., & Gjerloev, J. W. (2011). Evaluation of supermag auroral electrojet indices as indicators of substorms and auroral power. *Journal of Geophysical Research: Space Physics*, *116*(A12). https://doi.org/10.1029/2011JA016779

Nikitina, L., & Trichtchenko, L. (2021). Dynamics of electron flux in the slot region and geomagnetic activity. *Space Weather*, *19*(4), e2020SW002661. https://doi.org/10.1029/2020SW002661

O'Brien, T. P., Lorentzen, K. R., Mann, I. R., Meredith, N. P., Blake, J. B., Fennell, J. F., et al. (2001). Energization of relativistic electrons in the presence of ULF power and MeV microbursts: Evidence for dual ULF and VLF acceleration. *Journal of Geophysical Research: Space Physics*, *108*(A8). https://doi.org/10.1029/2002JA009784

Pinto, V. A., Bortnik, J., Moya, P. S., Lyons, L. R., Sibeck, D. G., Kanekal, S. G., et al. (2018). Characteristics, occurrence, and decay rates of remnant belts associated with three-belt events in the Earth's radiation belts. *Geophysical Research Letters*, *45*(22), 12099–12107. https://doi.org/10.1029/2018GL080274

Pokhotelov, D., Lefeuvre, F., Horne, R. B., & Cornilleau-Wehrlin, N. (2008). Survey of ELF-VLF plasma waves in outer radiation belt observed by cluster STAFF-SA experiment. *Annales Geophysicae*, *26*(11), 3269–3277. https://doi.org/10.5194/angeo-26-3269-2008

Pokhotelov, D., Rae, I. J., Murphy, K. R., Mann, I. R., & Ozeke, L. (2016). Effects of ULF wave power on relativistic radiation belt electrons: 8–9 October 2012 geomagnetic storm. *Journal of Geophysical Research: Space Physics*, *121*(12), 11766–11779. https://doi.org/10.1002/2016JA023130

Reeves, G. D., Spence, H. E., Henderson, M. G., Morley, S. K., Friedel, R. H. W., Funsten, H. O., et al. (2013). Electron acceleration in the heart of the Van Allen radiation belts. *Science*, *341*(6149), 991–994. https://doi.org/10.1126/science.1237743

Reiff, P. H., & Luhmann, J. G. (1986). Solar wind control of the polar CAP voltage. In Y. Kamide & J. A. Slavin (Eds.), *Solar wind magnetosphere coupling* (Vol. 126, pp. 453–476). https://doi.org/10.1007/978-90-277-2303-1_33

Reyes, P. I., Pinto, V. A., & Moya, P. S. (2021). Geomagnetic storm occurrence and their relation with solar cycle phases. *Space Weather*, *19*(9), e2021SW002766. https://doi.org/10.1029/2021SW002766

Rostoker, G. B. D., Skone, S., & Baker, D. N. (1998). On the origin of relativistic electrons in the magnetosphere associated with some geomagnetic storms. *AGU Geophysical Research Letters*, *25*(19), 3701–3704. https://doi.org/10.1029/98GL02801

Selesnick, R. S., Baker, D. N., Jaynes, A. N., Li, X., Kanekal, S. G., Hudson, M. K., & Kress, B. T. (2014). Observations of the inner radiation belt: Crand and trapped solar protons. *Journal of Geophysical Research: Space Physics*, *119*(8), 6541–6552. https://doi.org/10.1002/2014JA020188

Selesnick, R. S., Baker, D. N., Jaynes, A. N., Li, X., Kanekal, S. G., Hudson, M. K., & Kress, B. T. (2016). Inward diffusion and loss of radiation belt protons. *Journal of Geophysical Research: Space Physics*, *121*(3), 1969–1978. https://doi.org/10.1002/2015JA022154

Shprits, Y. Y., Kellerman, A., Aseev, N., Drozdov, A. Y., & Michaelis, I. (2017). Multi-mev electron loss in the heart of the radiation belts. *Geophysical Research Letters*, *44*(3), 1204–1209. https://doi.org/10.1002/2016GL072258

Silva, G. B. D., Alves, L. R., Tu, W., Padilha, A. L., Souza, V. M., Li, L.-F., et al. (2022). Modeling radiation belt electron dropouts during moderate geomagnetic storms using radial diffusion coefficients estimated with global MHD simulations. *Journal of Geophysical Research: Space Physics*, *127*(9), e2022JA030602. https://doi.org/10.1029/2022JA030602

Spence, H. E., Reeves, G. D., Baker, D. N., Blake, J. B., Bolton, M., Bourdarie, S., et al. (2013). Science goals and overview of the radiation belt storm probes (RBSP) energetic particle, composition, and thermal plasma (ECT) suite on NASA's Van Allen probes mission. *Space Science Reviews*, *179*(1), 311–336. https://doi.org/10.1007/s11214-013-0007-5

Spencer, E., Horton, W., Mays, M. L., Doxas, I., & Kozyra, J. (2007). Analysis of the 3–7 October 2000 and 15–24 April 2002 geomagnetic storms with an optimized nonlinear dynamical model. *Journal of Geophysical Research: Space Physics*, *112*(A4). https://doi.org/10.1029/2006JA012019

Srinivas, P. (2024). Pavithrags/WINDMImodel [model]. *Zenodo*. https://doi.org/10.5281/zenodo.11133963

Summers, D., Thorne, R. M., & Xiao, F. (1998). Relativistic theory of wave-particle resonant diffusion with application to electron acceleration in the magnetosphere. *Journal of Geophysical Research: Space Physics*, *103*(A9), 20487–20500. https://doi.org/10.1029/98JA01740

SuperMAG. (2023). SuperMAG SML dataset [Dataset]. http://supermag.jhuapl.edu/info/?page=acknowledgement

Thorne, R. M. (2010). Radiation belt dynamics: The importance of wave-particle interactions. *Geophysical Research Letters*, *37*(22). https://doi.org/10.1029/2010GL044990

Tsagouri, I., & Belehaki, A. (2023). Assessment of solar wind driven ionospheric storm forecasts: The case of the solar wind driven autoregression model for ionospheric forecast (SWIF). *Advances in Space Research*, *72*(12), 5577–5586. https://doi.org/10.1016/j.asr.2022.06.047

Turner, D., Shprits, Y., Hartinger, M., & Angelopoulos, V. (2012). Explaining sudden losses of outer radiation belt electrons during geomagnetic storms. *Nature Physics*, *8*(3), 208–212. https://doi.org/10.1038/nphys2185

Turner, D. L., Kilpua, E. K. J., Hietala, H., Claudepierre, S. G., O'Brien, T. P., Fennell, J. F., et al. (2019). The response of Earth's electron radiation belts to geomagnetic storms: Statistics from the Van Allen probes era including effects from different storm drivers. *Journal of Geophysical Research: Space Physics*, *124*(2), 1013–1034. https://doi.org/10.1029/2018JA026066

WDC. (2023). World data center for geomagnetism, Kyoto dataset [Dataset]. http://wdc.kugi.kyoto-u.ac.jp/aeasy/index.html

Zhang, J., Richardson, I. G., Webb, D. F., Gopalswamy, N., Huttunen, E., Kasper, J. C., et al. (2007). Solar and interplanetary sources of major geomagnetic storms (*Dst* 100 nt) during 1996–2005. *AGU Geophysical Research: Space Physics*, *112*(A10). https://doi.org/10.1029/2007JA012321